Influence of the porosity and type of bioglass on the micro-mechanical and bioactive behavior of coated porous titanium substrates

R. Moriche[1], A. M. Beltrán[1,*], B. Begines[2], J. A. Rodríguez-Ortiz[1], A. Alcudia[2] and Y. Torres[1,*]

[1] Departamento de Ingeniería y Ciencia de los Materiales y el Transporte, Escuela Politécnica Superior, Universidad de Sevilla, Sevilla, Spain

[2] Departamento de Química Orgánica y Farmacéutica, Facultad de Farmacia, Universidad de Sevilla, Sevilla, Spain

*Corresponding authors (abeltran3@us.es and ytorres@us.es)

Abstract

In this study, the best equilibrium among adherence, micro-mechanical properties and coating bioactivity of bioactive glasses (45S5 and 1393) on porous titanium substrates has been explored and their potential uses for bone tissue implants. Porous titanium discs with different porosities (30 and 60 vol. %) and pore size distributions (100-200 and 355-500 μm) were utilized to rationalize their influence on both properties and performance. It was corroborated that porous samples produced a reduction in micro-hardness (~ 2000-4000 N/mm^2) and the elastic modulus (~ 25-50 GPa), obtaining values closer to those of human bones, as well as induced a beneficial role to integrate the coatings. On one hand, bioglass 1393 presented greater capacity for pore infiltration while 45S5 was more bioactive. The results explained the better adherence and microhardness for bioglass 1393 and the significant formation of hydroxyapatite and calcium phosphates of bioglass 45S5, confirmed by ^{29}Si MAS NMR.

Keywords: bioglass; porous titanium; micro-mechanical properties; bioactivity; hydroxyapatite.

1. Introduction

Titanium (Ti) and its related alloys have been widely used as biomaterials for bone tissue implants, but, despite of their high biocompatibility, there are some issues that still remains a challenge, such as tailoring their stiffness and/or improving osseointegration [1,2]. In order to enhance the biomechanical performance of Ti-based implants, related to stress-shielding phenomenon, and to replicate the cortical bone tissue structure, porous substrates manufactured of Ti alloys have been considered [3]. K. Bari et al. [4] proposed several designs, with porosities ranging from ~ 55 up to ~ 74%, which exhibit Young's modulus and bearing strength close to the ones of human bone, validating their potential use as scaffolds. C. Chen et al. [5] also described a porous Ti6Al4V cage inhibiting stress-shielding due to the fact that porosity reduces the elastic modulus in comparison with fully-dense implants.

On the other hand, the use of bioactive coatings have been widely investigated to improve osseointegration [6]. Particularly, bioactive glasses (BGs) were developed in the 1970s and they are based on silicates coupled with other minerals, which are present in the human body [7]. One of the advantages of these materials is their capability to bond them to soft and hard tissues, as well as favoring the growth and regeneration of bone tissue [8,9]. Among the most common BGs, those denominated 45S5 and 1393 (BG 45S5 and BG 1393, respectively) are widely employed due to their properties. It has been reported that BG 1393 has lower viscosity and tendency to crystallize during sintering than BG 45S5, which can be advantageous to retain bioactivity [10]. Additionally, the release of ions from bioactive glasses into the human fluids promotes stimulation of angiogenesis and wound healing [11,12], which is very suitable if BGs are used as coating on metallic implants or fillers in polymeric matrices [13,14].

Based on the challenges needed to be solved in Ti-based implants, the aim of this work was to find the best equilibrium between achieving the best adherence, micro-

mechanical properties and bioactivity of the BG coatings/porous commercially pure titanium systems. The influence of porosity and chemical composition of the bioactive glass was investigated using two different BGs. Additionally, to elucidate the influence of the pore size distribution of the substrates, two ranges of porosities (30 and 60 vol. %) with pore size distributions of 100-200 and 355-500 µm, were investigated.

2. Materials and methods

2.1. Materials

Commercially pure grade 4 titanium (c.p. Ti) powder was purchased from *SEJONG Materials Co. Ltd.* (Seoul, Korea). The spacer particles used to manufacture the porous substrates was NH_4HCO_3 with a purity of 99% and was acquired from *Cymit Química S.L* (Spain). Two different size distributions of the spacer particles were utilized to analyze their influence on the properties, which were 100-200 and 355-500 µm [15]. Also, two BGs of different compositions (see Table 1) were used for coating Ti substrates. The two bioglasses, BG 45S5 and BG 1393, were obtained from *SCHOTT Vitrixx®*. The $d_{[50]}$ of BG 45S5 and BG 1393 powders was 4.5 and 6.1 µm, respectively, and both of them were used as received as the amorphous form.

Table 1. Composition of the bioglasses

Bioglass	SiO_2 (mol%)	CaO (mol%)	Na_2O (mol%)	P_2O_5 (mol%)	K_2O (mol%)	MgO (mol%)
45S5	60	20	18	2	--	--
1393	54.3	22.2	6.2	1.9	8	7.4

2.2. Manufacture of porous titanium substrates coated with BGs

Porous and fully-dense c.p. Ti substrates were obtained by the space-holder (SH) technique and conventional powder metallurgy (PM), respectively. The detailed

procedure has been previously reported by the authors of this work [16,17]. Although the route to generate porosity was the same, porous substrates were diverse and could differently behave. In the present study, two different porosities (30 and 60 vol. %) were compared as well as two spacer particles size distributions (100-200 and 355-500 μm), er to evaluate their influence in micro-mechanical properties, infiltration capability, bioactivity and adherence. Prior to the deposition of the coatings, the surface of the substrates was polished, ensuring no modification of the porosity of c.p. Ti samples. Both BG coatings were prepared using the dripping-sedimentation deposition technique with a suspension of BG/ethanol (10 mg/ml). So, 1 ml of the suspension was deposited onto the surface and, after 24 h at room temperature, the ethanol was evaporated. This procedure was repeated twice. A thermal treatment at 700 ºC, 1 h and 820 ºC, 5 s, both at 10^{-2} mbar, for 1393 and 45S5 bioglasses, respectively, was performed to sinter BG coatings in a *Vita Vacumat 6000 M* furnace. The above mentioned temperatures and time of the thermal treatment was fixed according to the recommendations of the furnace manufactures for these BGs and considering their phases diagram to avoid the compaction of the BG powder.

2.3. Chemical, microstructural and micromechanical characterization

Microstructural characterization of the samples was carried out by optical microscopy and scanning electron microscopy (SEM) by using a *Nikon Eclipse MA100N* and a *FEI TENEO* microscope, respectively.

The apparent density of the substrates was obtained by the Archimedes' method following the ASTM C373-14 standard [18] and from the optical micrographs by quantitative image analysis. This method has been previously reported by the authors corroborating its adequacy to evaluate samples with uniformly distributed pores.

Besides, it is scalable to industrial production. Additionally, from quantitative image analysis, the mean free path between pores was also calculated to determine position of indentations, as it will be explained below.

The micro-mechanical behavior of the BG coated samples was studied by using instrumented micro-indentation to determine how porosity (vol. % and pores size) influences the micro-hardness and elastic modulus at the microscale. Static loading-unloading tests were performed in a *Microtest* machine (*MTR3/50-50/NI*) using a Vickers indenter. A preload of 0.1 N was used to ensure the contact between the indenter and the surface and the maximum load in micro-mechanical tests was 1 N. The maximum load was defined based on a previous published work of the authors [19]. Also, although results were not included in this work, additional tests were carried out at higher loads to verify that 1 N was enough to obtain representative values on the stabilized region [20] of hardness and elastic modulus in porous c.p. Ti, avoiding pileup and the appearance of chipping of the BGs coatings. This maximum load was applied with a rate of 0.5 N/min and a dwell time of 40 s. It is important to point out that, in uncoated substrates, indentations were performed on the porous c.p. Ti matrix, at the center of an area among pores with dimensions equal to the calculated average mean free path. At least, five indentations were performed in each sample to obtain the average values.

Micro-hardness and Young's modulus were measured from the resulting loading-unloading curves by using the Oliver and Pharr method [21]. Following this method, micro-hardness (*H*) was calculated according to equation (1):

$$H = \frac{P_{max}}{A} \qquad (1)$$

where P_{max} is the maximum load and A is the contact area calculated from the depth of contact between the indenter and the sample surface. The effective elastic modulus (E_{eff}) was calculated from expression (2):

$$E_{eff} = \frac{S}{\beta \dfrac{2}{\sqrt{\pi}} \sqrt{A}} \tag{2}$$

where S is the slope of unloading P-h curve and β is a correction factor dependent on the indenter. The elastic modulus was calculated from E_{eff} considering the elastic modulus (E_i) and the Poisson's ratio of the indenter (ν_i) and the tested material (c.p. Ti) (ν) following equation (3):

$$E = \frac{(1 - \nu^2)}{1/E_{eff} - (1 - \nu_i^2)/E_i} \tag{3}$$

2.4. Characterization of the presence of hydroxyapatite

With the aim of evaluating bioactivity of coated samples, the hydroxyapatite (HA) forming ability of the coatings in simulated body fluid (SBF) was assessed following the standard ISO 23317-2014 [22]. Tests were performed at a temperature of 36.5 ± 2.0 °C. The SBF solution was renewed after 7, 14 and 21 days and coated substrates were analyzed at 14 and 21 days to evaluate HA formation and deposition.

Following the standard recommendations, the SBF composition was determined prior and after tests using inductively coupled plasma atomic emission spectrometry (ICP) Horiba Jobin Yvon. The characterization techniques proposed in the standard methodology used, and additionally reported in other similar studies, to analyze the formation of hydroxyapatite were applied in this work to determine and discuss HA formation. X-ray diffraction (XRD) and SEM observation of dried samples were employed to detect the formation of the different phases, while solid-state nuclear

magnetic resonance (NMR) was carried out to study the proportion of non-bridging oxygen, since it is directly related to the HA crystallization [23].

In order to corroborate the formation of HA, the surface of the coated samples was characterized by SEM using the same equipment indicated above and their composition was determined by energy dispersive X-ray analysis (EDS-SEM) and thin film X-ray diffraction (TF-XRD) following the mentioned standard. TF-XRD was conducted in a *Bruker diffractometer D8 Advance A25* with a Cu Kα radiation of 0.154 nm.

As it has been mentioned, to predict the bioactivity of both BGs, network connectivity (NC) were estimated in each case. Although NC is theoretically described according to the chemical composition of the glass (Equation 4), it has also been experimentally defined considering the silicon environments (Q^n) that establish the chemical structure of the corresponding BG [24], characterized by ^{29}Si magic angle-spinning solid-state nuclear magnetic resonance (MAS NMR) (Equation 5).

$$NC_T = \frac{(4 \times SiO_2) + (6 \times P_2O_5) - (2 \times CaO)}{SiO_2} \tag{4}$$

$$NC_{NMR} = Q^1 + (2 \times Q^2) + (3 \times Q^3) + (4 \times Q^4) \tag{5}$$

A *Bruker Avance III 600 MHz WB* spectrophotometer was employed to perform the ^{29}Si MAS NMR spectra on the raw pulverized BGs. A single pulse length of 75º and a relaxation time of 15 s where used on samples spun at 10 kHz. Tetramethylsilane were applied as a reference for chemical shifts. Finally, DMfit software was utilized to conduct spectra deconvolution.

3. Results and discussion

Before coating procedure, all the substrates were characterized to evaluate the microstructure and micro-mechanical behavior by *P-h* curves (section 3.1). Then, the

coating (BG 1393 or BG 45S5) were deposited and the samples were analyzed in terms of micro-mechanical properties and bioactivity.

3.1. Microstructure and micro-mechanical properties of c.p. Ti porous substrates

Since porosity can strongly affect the micro-mechanical properties of the c.p. Ti substrates and, consequently, coated samples behavior; the microstructure and micro-mechanical properties of the substrates as a function of porosity and pores size distribution were discussed.

Figure 1 shows representative SEM images of fully-dense and porous c.p. Ti substrates. The geometry of the pores, the size distribution and the volume fraction of the porous Ti substrates were in accordance with the spacer particles used to generate the porosity via SHT [17]. From the SEM micrographs it could be observed that the inner surfaces of the pores were rough, which could be advantageous to promote the adherence of BGs coatings on the inner walls of the open pores, as well as to increase bioactivity because of the higher specific surface area [25].
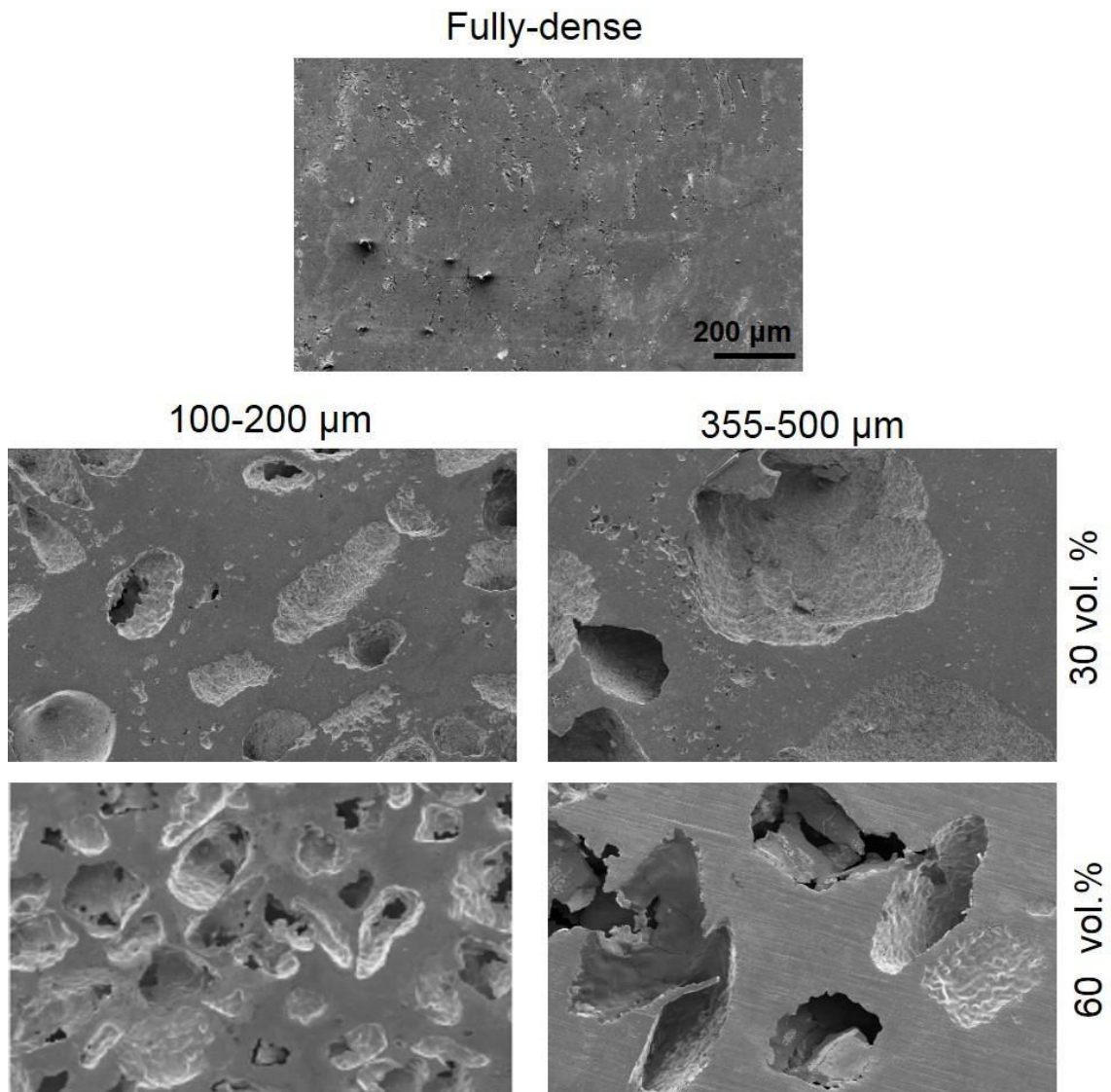
Figure 1. SEM images of surfaces of fully-dense and porous c.p. Ti substrates. Common scale bar.

To further characterize the porosity of the substrates, Figure 2 displays some parameters related to porosity after sintering, which were calculated from the Archimedes' and geometrical methods: apparent density, total and interconnected porosity. These properties were plotted as a function of the volume fraction and spacer particles size distribution used in the SHT. It is important to note that the range of porosities and size distributions of all the resultant substrates were in the range of those of human bones, i.e. a porosity between 30-80 % and a pore size distribution of 100–600 µm [26].

From the results, it was observed that there was a slight difference in apparent density obtained by geometrical and Archimedes' method. When the apparent density was determined by the Archimedes' method, it was more evident the interconnected porosity, as open porosity can be filled. This is important in implants because open and interconnected porosity is advantageous to make possible the nutrient transport, bone cell ingrowth and differentiation [27].
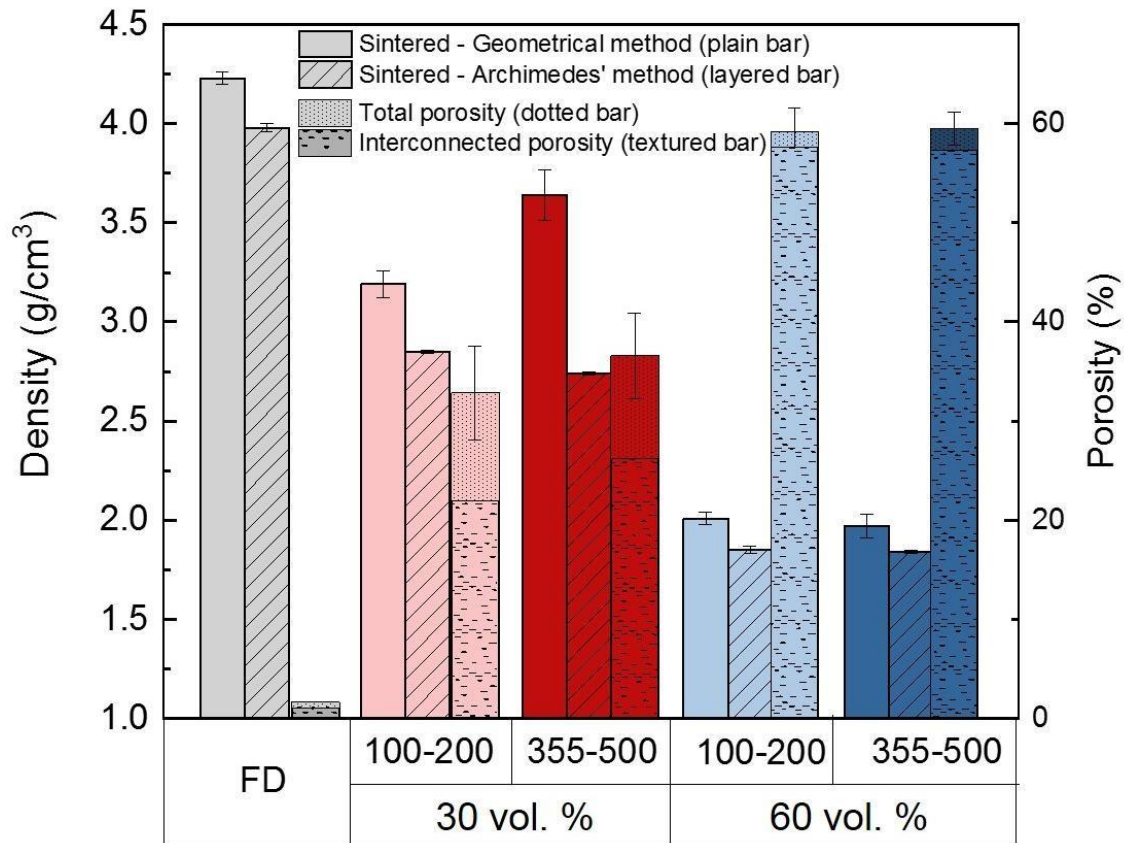

Figure 2. Density (geometrical and Archimedes' method) and porosity (total and interconnected) of c.p. Ti substrates. Influence of the measure method and process parameters (porosity and space-holder size distribution). Note: Fully-dense (FD); space-holder size distribution is in μm.

Once this fact has been clarified, results showed that the relative density of sintered substrates was, as expected, dependent on the space-holder content and its size distribution. These tendencies could be related to the compaction capability and the specific surface area of the c.p. Ti powder, which was fundamental for sintering. As a

result, it was confirmed that the used space-holder technique constitutes an effective process to obtain tunable porosity in c.p. Ti substrates, which can be selected depending on the human bone part to be replaced. In this context, the manufactured substrates with micrometric and interconnected pores may not only favor the infiltration and adherence of the BG coating but can also compromise the micro-mechanical behavior as the mechanical strength can be considerably reduced [28].

With the aim of elucidating this influence in micro-mechanical properties, representative *P-h* curves from tests performed on the c.p. Ti substrates are shown in Figure 3a. Additionally, the values of the micro-mechanical properties and parameters are depicted in Table 2. The obtained results allowed affirming that the maximum penetration depth and the elastic recovery were lower in the fully-dense substrate, which means a higher stiffness and micro-hardness. In addition, the calculated micro-hardness and elastic modulus (Figure 3b) slightly decreased with a higher porosity, but increased with the pores size distribution, being more similar to fully-dense c.p. Ti, in contrast with the elastic recovery. The observed tendency was due to the higher mean free path obtained for both lower porosity (30 vol. %) and bigger pore size (355–500 μm) as the c.p. Ti matrix was more continuous and, consequently, the c.p. Ti area between pores was larger. This fact has been already reported by X. Ma et al. [26] in porous NiTi alloys, which were tested under uniaxial compression.
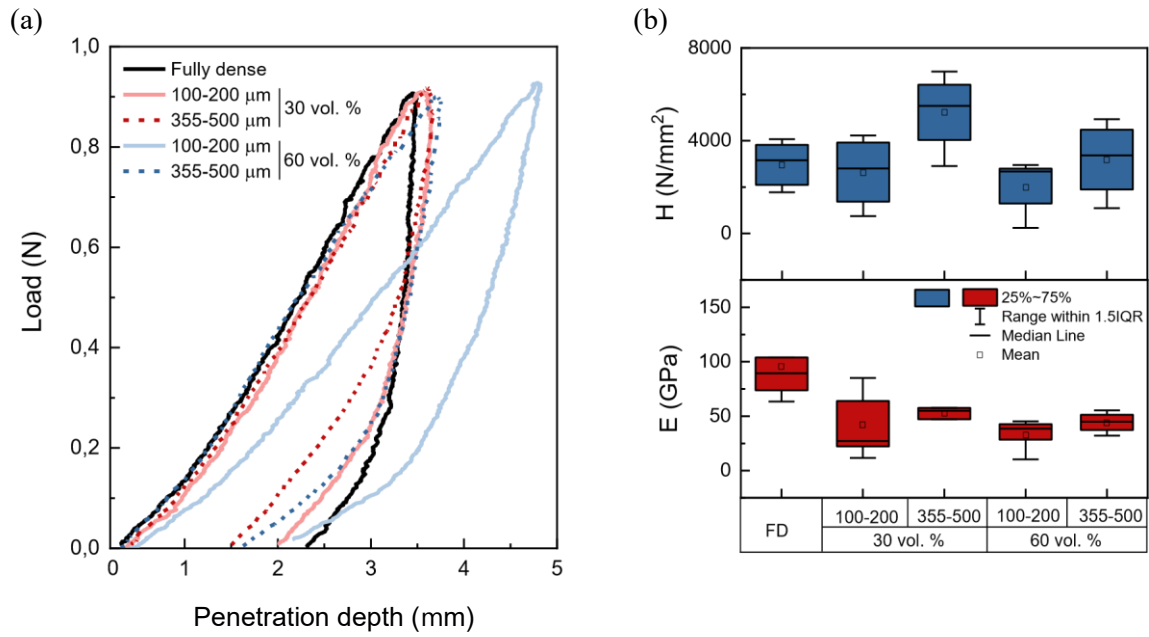
Figure 3. Micro-mechanical properties of c.p.-Ti substrates: (a) representative *P-h* curves and (b) micro-hardness (*H*) and elastic modulus (*E*). Note: Fully-dense (FD); space-holder size distribution is in μm.

Table 2. Characteristic parameters calculated from *P-h* curves for c.p. Ti substrates.

Substrates		Mean free path (μm)	Penetration depth (μm)		Elastic recovery	
			Maximum	**Permanent (unloaded)**	**Absolut (μm)**	**Relative (%)**
Fully-dense		-	3.0	2.0	0.9	31.9
30 vol. %	**100-200 μm**	238 ± 20	3.5	2.1	1.4	39.4
	355-500 μm	520 ± 41	3.6	1.6	2.0	55.1
60 vol. %	**100-200 μm**	203 ± 13	4.7	2.2	2.5	52.4
	355-500 μm	320 ± 27	3.6	1.7	1.9	52.7

To clarify the influence of the mean free path in porous c.p. Ti substrates, Figure 4 shows the maximum penetration as a function of the mean free path. When the mean free path of the c.p. Ti matrix among pores decreased, micro-hardness also did it and the maximum penetration depth increased. Therefore, it could be concluded that there was a higher influence of the pores in the vicinities. As the area of c.p. Ti free of pores enlarged, the mechanical curve looked more like the one of the fully-dense c.p. Ti.
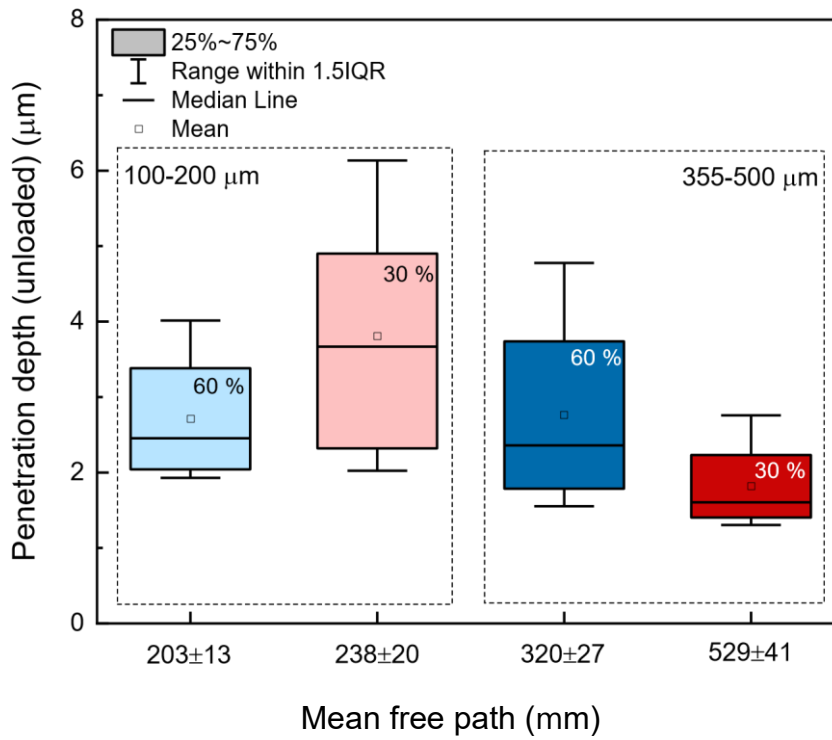
Figure 4. Penetration depth calculated from *P-h* curves (once unloaded) as a function of the mean free path between pores of c.p. Ti substrates.

3.2. Chemical characterization, microstructure and micro-mechanical properties.

The chemical structure of the different silicon environments in a bioglass is directly related to its potential bioactivity [29]. To predict differences in the bioactivity of the raw BG 45S5 and BG 1393, the network connectivity of each bioglass was determined both theoretical and experimentally. At atomic level, the network connectivity is closely correlated to the different silicon environments, that are noted as Q^n (where $n = 4,3,2,1$), depending on the number of non-bridging oxygen (NBO) bound to the silicon atom under study (Si*) [30]. Thus, a Q^4 environment corresponds to a silicon atom with no NBO bound to it [Si*(OSi)$_4$]. A Q^3 environment implies a Si* atom bound to (OSi)$_3$ and a NBO [(NBO)Si*(OSi)$_3$] while Q^2 and Q^1 represent (NBO)$_2$Si*(OSi)$_2$ and (NBO)$_3$Si*(OSi)$_1$, respectively. According to their chemical composition, NC$_T$ of both

BGs and therefore their bioactivities are similar, showing values of 3.2 and 3.4 (Table 3) for BGs 45S5 and 1393, respectively. However, while theoretical NC only considers the proportions of the ternary system $SiO_2/P_2O_5/CaO$ present in the BG, ^{29}Si MAS NMR studies can elucidate the real chemical structure of the glass network, resulting in an experimental value of NC. Thus, Figure 5a shows both chemical shifts appeared for the different silicon environments of BG 45S5. In particular, commercially available BG 45S5 displayed a clear strong influence of Q^2 and Q^3 environments, with chemical shifts appearing at approximately -80 and -87 ppm, respectively, that was supported by data previously described in the literature [31]. Spectra deconvolution resulted in a contribution of a 36% of the Q^3 environment and a 64% attributed to the Q^2 environment (Table 3). However, BG 1393 (Figure 5b) displayed a chemical shift displacement corresponding to a higher polymerized silicon network, with a signal with major contribution of a Q^4 environment, appearing at -110 ppm, and a Q^3 environment at -100 ppm. Deconvolution of BG 1393 signal revealed a contribution of a 48% assigned to the Q^4 environment while the 52% represents to the Q^3 environment. These contributions correspond to a NC_{NMR} of 2.4 and 3.5 (Table 3) for BGs 45S5 and 1393, respectively, demonstrating that the chemical network adopted by BG 45S5 favors its bioactivity when compared to BG 1393 [32,33].
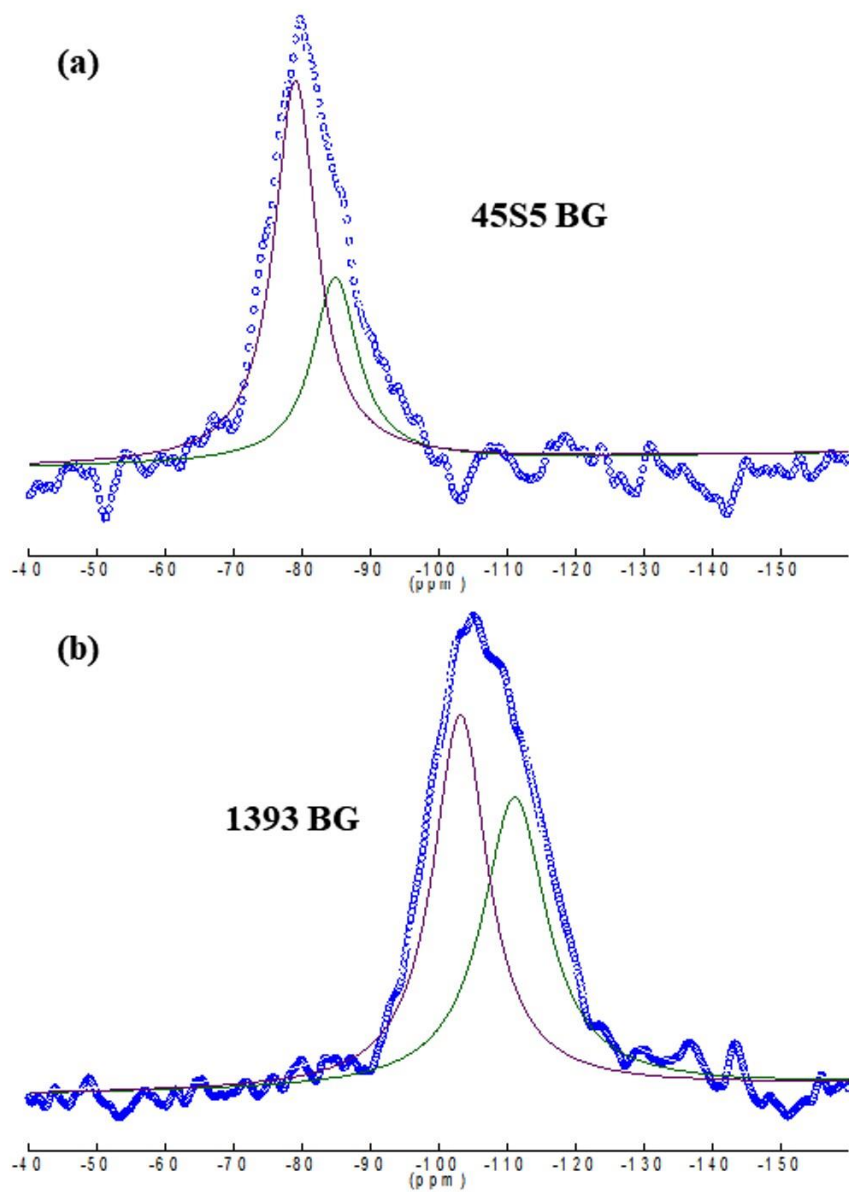
Figure 5: MAS NMR spectra of (a) 45S5 and (b) 1393 BGs with their corresponding

deconvolution.

Table 3. Network connectivity and different silicon environments contributions for each

BG.

BG	N		Q^n environments (%)			
	Theoretical	NMR	Q^1	Q^2	Q^3	Q4
45S5	3.2	2.4	-	64	36	-
1393	3.4	3.5	-	-	52	48

After analyzing the chemical structure of BGs, macro- and microstructural features of coatings were discussed. Figure 6 shows macrographs of the BGs coated samples before and after the vitrification process. The coatings covered all the surface of the c.p. Ti substrates and penetrated in open porosity. Additionally, the adherence of the BG 1393 improved respect to BG 45S5, being poor in the case of fully-dense c.p. Ti. The lack of adherence of the coating on fully-dense substrates detected at macroscopic scale may be related to the infiltration of BGs inside the pores where they were anchored. Therefore, coated fully-dense samples were not included.

Besides, due to the lower coefficient of thermal expansion (CTE) of BG 1393, which is more similar to the one of the c.p. Ti ($8.9 \cdot 10^{-6}$ ${}^{o}C^{-1}$) [34,35], samples coated with this type of BG showed improved adhesion. In contrast, BG 45S5 coatings presented lower adherence, which could be attributed to the larger difference in thermal expansion coefficient respect to the substrate, being $15.1 \cdot 10^{-6}$ ${}^{o}C^{-1}$ in the case of the BG 45S5 [36], and the possible crystallization of the BG 45S5 [37], which will be analyzed below by XRD. Furthermore, the adhesion of the BGs coatings was enhanced in porous substrates due to the mechanical anchoring because of the interconnected porosity, already discussed, and roughness of the inner surface of the pores.

Although a better adherence was achieved in porous substrates, the homogeneity of the BGs coatings was improved in the case of lower porosity (30 vol. %) and smaller size distributions (100-200 µm). Additionally, a crucial issue to point out was the fact that the surface roughness of the sintered coatings diminished when a second layer was added to the system, probably due to a complete filling of the pores.

In c.p. Ti substrates with a bigger pore size distribution and higher interconnectivity, the infiltration of the BG into the metallic substrate was favored. This resulted in a rougher surface, as BG can further penetrate the substrate due to the mentioned interconnectivity between pores (section 3.1).
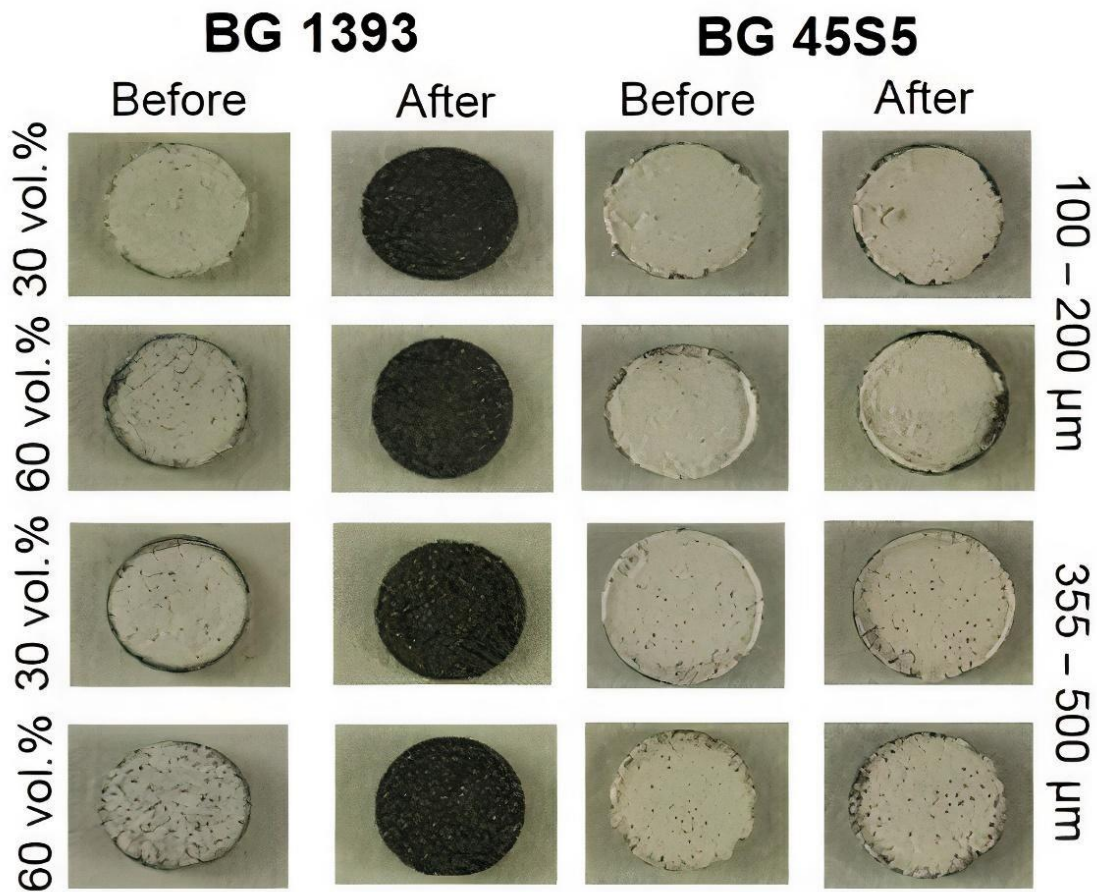
Figure 6. Macrographs of the BG coated c.p. Ti substrates once deposited and before and after thermal treatment. (Fully-dense c.p. Ti coated samples are not included due to the low adherence). Diameter of the samples ∼ 11 mm.

Once macroscopic features have been discussed, microstructure and morphology of BGs coatings was studied. Figure 7 shows representative micrographs of the different coatings after vitrification. Signs of fusion, i.e., micro-cavities due to shrinkage and smooth surfaces characteristic of a vitreous phase, could be observed for BG 1393 coatings. In Figure 7b, micro-cracks due to shrinkage could be appreciated in BG 1393 coatings, which seemed to be initiated in the pores of the BG coating [38]. In contrast, BG 45S5 coatings presented a rough surface with micro-pores uniformly distributed creating a coral-like structure.
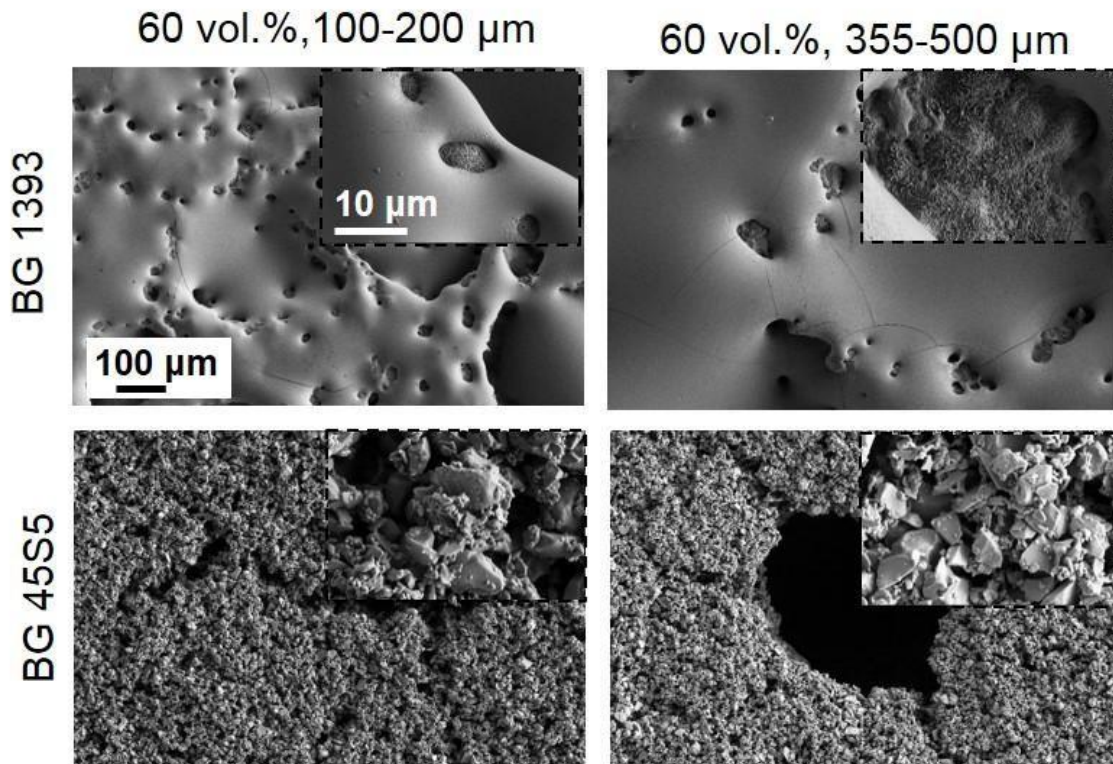
Figure 7. SEM images of BG analyzed coatings. Influence of the substrate (percentage of porosity, 30 vol. % and 60 vol. %, and pore size distribution, 100-200 and 355-500 μm) and the composition of the coating. Inset: details of the surface at higher magnification. Common scale bars.

The thickness and penetration of the BGs into the porous structure were also analyzed by SEM. Representative SEM micrographs of the cross-section of BG-coated c.p. Ti are shown in Figure 8. The thickness of BG 45S5 was ~70 μm thick (Figure 8a and 8b) and for BG 1393 coatings it was less than 40 μm (Figure 8c), being more difficult to observe since it has penetrated into the substrates. Even in this case, it presented a uniform dense morphology and smooth surface (Figure 8c). In contrast, as it was mentioned above, BG 45S5 coatings showed higher micro-porous and roughness, with homogeneous thickness along the surface of the substrates. These micrographs also evidenced differences of the coatings inside pores. Interestingly, BG 1393 melted quicker and better and it always filled the pores, independently of the pore size range, while BG 45S5 was be able to infiltrate the larger pores.
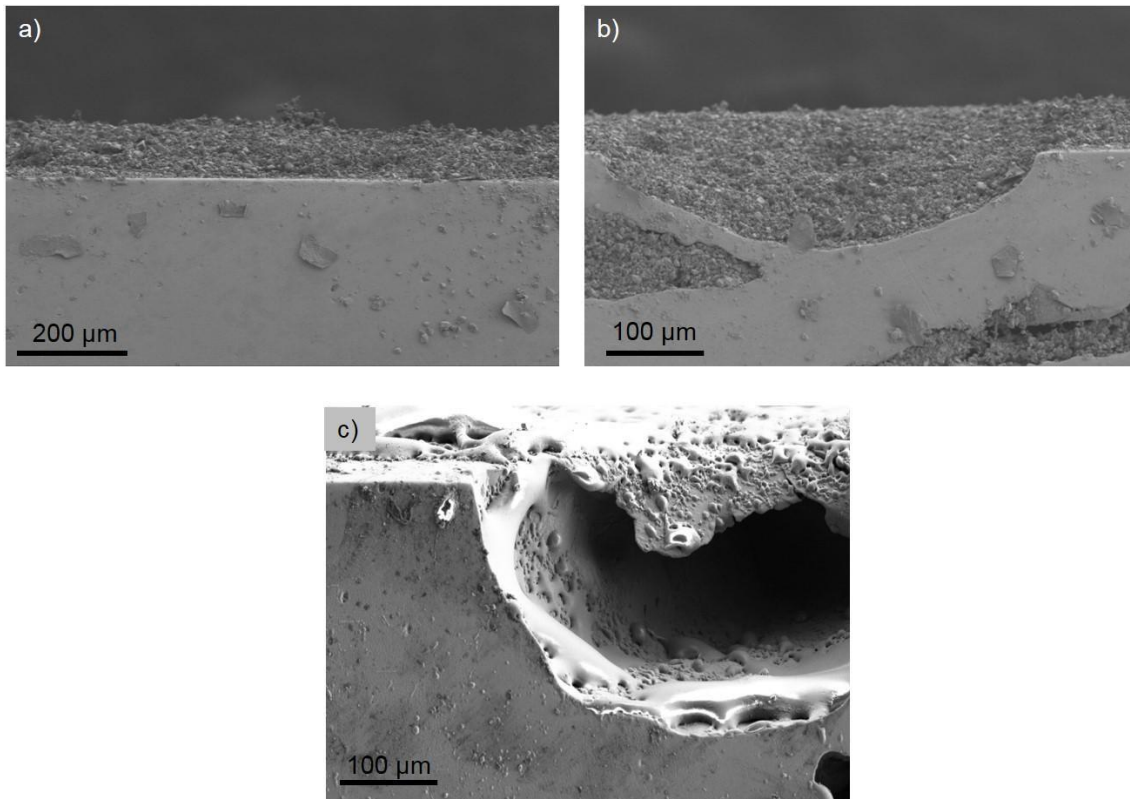
Figure 8. SEM images of the cross-section of the two BGs coatings on the c.p. Ti substrates with 30 vol. % of porosity and pore range size 355-500 µm. (a, b) BG 45S5 and (c) BG 1393.

Micro-mechanical properties were tested after the deposition of the coatings to study the effect of the BGs on the micro-mechanical properties of the surface. Although mechanical properties measured by compression tests have been already published [39], a micro-mechanical analysis of the coated c.p. Ti surface with the corresponding BGinduced modifications needs to be assessed. Figures 9a and 9b, and Table 4 show the micro-mechanical (*P-h*) curves and the main parameters obtained from the mentioned curves, respectively. These results confirmed the fact that, independently on the characteristics of the porous substrates, the micro-hardness and the elastic recovery in

BG 45S5 coatings were lower (less penetration depth) than BG 1393. This could be attributed to the noticeable presence of micro-porosity and the poor adherence of the

coatings due to the higher discrepancy between the thermal expansion coefficients already discussed. It is important to highlight that the existence of cavities and microcracks due to shrinkage as well as the absence of pores and smooth surface explained the micro-mechanical behavior of BG 1393 coatings and the values of the elastic recovery.

To study the influence of porosity and pores size distribution in the micro-mechanical properties of coated samples, Figures 9c and 9d show the calculated H and E for all the coated substrates. It can be elucidated that both, H and E, were superior in the case of using BG 1393 coatings. This fact could be attributed to the chemistry, structure and morphology of the BGs coatings [16,40], though BG 1393 coatings presented a dense layer (Figures 8a and 8b), 45S5 coatings resulted in a coral-like structure similar to a cellular morphology, which results in the stated relatively low micro-mechanical properties. Additionally, BG 45S5 coatings in substrates with bigger pores size distributions and higher porosities showed lower mechanical properties since pores were filled with the corresponding BG and the probability of indenting in these regions was higher. On the contrary, BG 1393 coatings, because of their high micro-mechanical performance, induced an increase of the micro-hardness and elastic modulus due to the better interfacial strength.
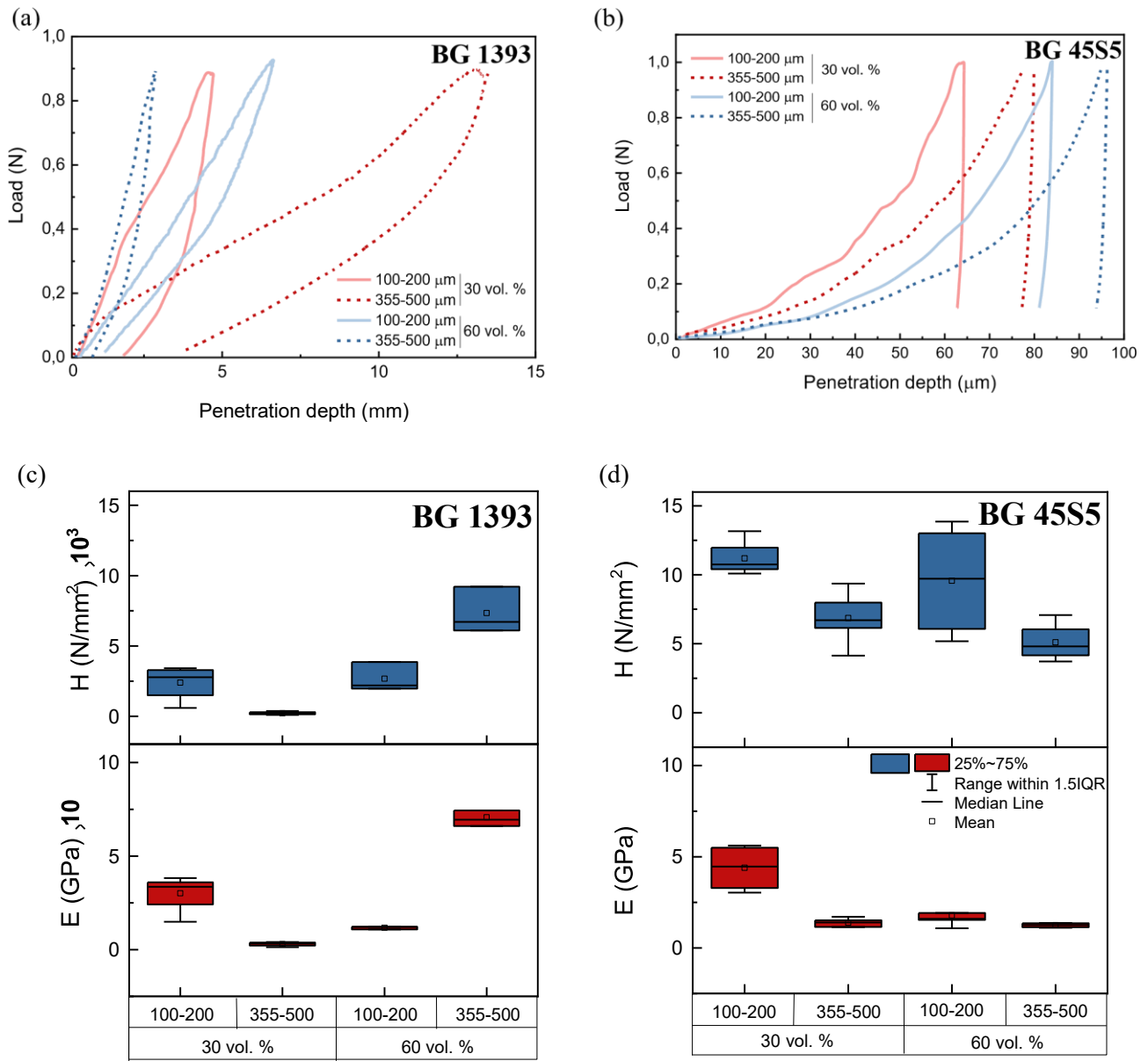
Figure 9. Micro-mechanical properties of BG coated c.p. Ti substrates: (a, b) representative P-h curves and (c, d) micro-hardness (*H*) and elastic modulus (*E*) of (a, c) BG 1393 and (b, d) BG 45S5 coatings.

Table 4. Characteristic parameters calculated from *P-h* curves for BGs coated c.p. Ti substrates (space-holder size distribution in µm).

BG	Substrates		Penetration depth (µm)		Elastic recovery	
			Maximum	**Permanent (unloaded)**	**Absolut (µm)**	**Relative (%)**
1393	**30%**	**100-200**	6.9	3.3	3.6	52.2
		355-500	12.9	3.6	9.3	72.1

	60%	100-200	6.9	1.6	5.3	76.8
		355-500	2.5	0.9	1.6	64.0
45S5	30%	100-200	62.2	61.3	0.9	1.4
		355-500	79.7	77.5	2.2	2.8
	60%	100-200	90.5	88.5	2	2.2
		355-500	77.1	75.5	1.6	2.1

3.3. Hydroxyapatite formation of BGs coated c.p. Ti porous substrates

With the aim of analyzing the enhancement in HA formation promotion, SBF tests were performed and results were evaluated in terms of the composition of the coatings and the SBF solution after 14 and 21 immersion days. These studies were performed for all the porous substrates coated with BG 1393 or BG 45S5 and the fully-dense sample, which was taken as a reference.

Table 5 shows the composition of the SBF for the initial state and after 14 and 21 days of immersion. A reduction of Ca and P was observed due to the precipitation of calcium phosphates on the studied surfaces. Additionally, the Si content significantly increased after 14 days in BG 45S5 coated samples, which could be attributed to a partial solution of this BG while calcium phosphates were formed [41]. It is important to note that the Si content after 21 days seemed to be lower in both BGs, as the SBF was renewed and the quantity of remaining bioglass decreased, as well as the Si content. Therefore, after 21 days, the dissolution of the bioglass stabilized, reaching an equilibrium.

Table 5. Chemical composition of SBF by ICP. Influence of the porosity and BG coating in HA formation (space-holder size distribution is in µm).

mg/L	0 days in SBF	BG 45S5										BG 1393				
		14 days in SBF					21 days in SBF									
		FD	30 vol. %		60 vol. %		FD	30 vol. %		60 vol. %		FD	30 vol. %		60 vol. %	
			100-200	355-500	100-200	355-500		100-200	355-500	100-200	355-500		100-200	355-500	100-200	355-500
Ca	74.3	59.6	56.7	57.8	62.1	62.2	52.6	53.4	51.6	59.0	60.8	66.6	63.8	65.4	73.0	72.7
P	39.2	12.0	11.9	10.2	12.2	14.5	22.8	23.5	22.2	28.1	29.3	32.5	32.2	32.4	38.8	39.2
Si	≤ 0.04	43.0	39.7	44.9	46.3	37.9	1.29	1.9	2.4	16.8	0.6	2.2	1.0	2.4	0.7	1.0
Ti	≤ 0.004															

Note: Fully-dense (FD)

Comparing the results after 21 days for a same pore size distribution, the diminution of Ca and P in SBF was more pronounced for lower porosities (30 vol. %). Additionally, for the same porosity, the difference in Ca and P content was less significant, showing that the range of porosity had higher influence than the pores size distribution. Related to the composition of the BGs coating, samples coated with BG 45S5 seemed to promote the reduction of Ca and P in SBF.

Structural and compositional modifications on the surface after 21 days in SBF were analyzed by SEM (Figure 10). All the SEM images showed changes of the surface topography, caused by the presence of HA, as it was detected by EDS-SEM (Table 6) and XRD (Figure 11). It is worth to mention that BG 45S5 coatings showed a crystalline structure, sodium calcium silicate crystals (i.e., $Na_2CaSi_2O_6$), due to its higher tendency to crystallize compare to BG 1393, which were amorphous, [36]. It is important to note that, although BG 45S5 crystallized after the thermal treatment, it did not cause the loss of bioactivity [42].

Although the roughness of the surface made difficult quantifying atom contents by EDS-SEM, the presence of regions rich in Ca and P could predict the formation of calcium phosphates with different Ca/P ratios [12,43]. The values for the studied samples are included in Table 6. The substrate with 60 vol. % porosity and smaller pores

size) coated by BG 45S5 presented a Ca/P of 1.64 very close to 1.67, which is associated to the natural HA [44]. Higher porosities induced a reduction of the Ca/P ratio. In contrast, the influence of the pores size distribution did not follow the same tendency for both BGs and porosities, which can be attributed to the different morphology adopted on the surface.
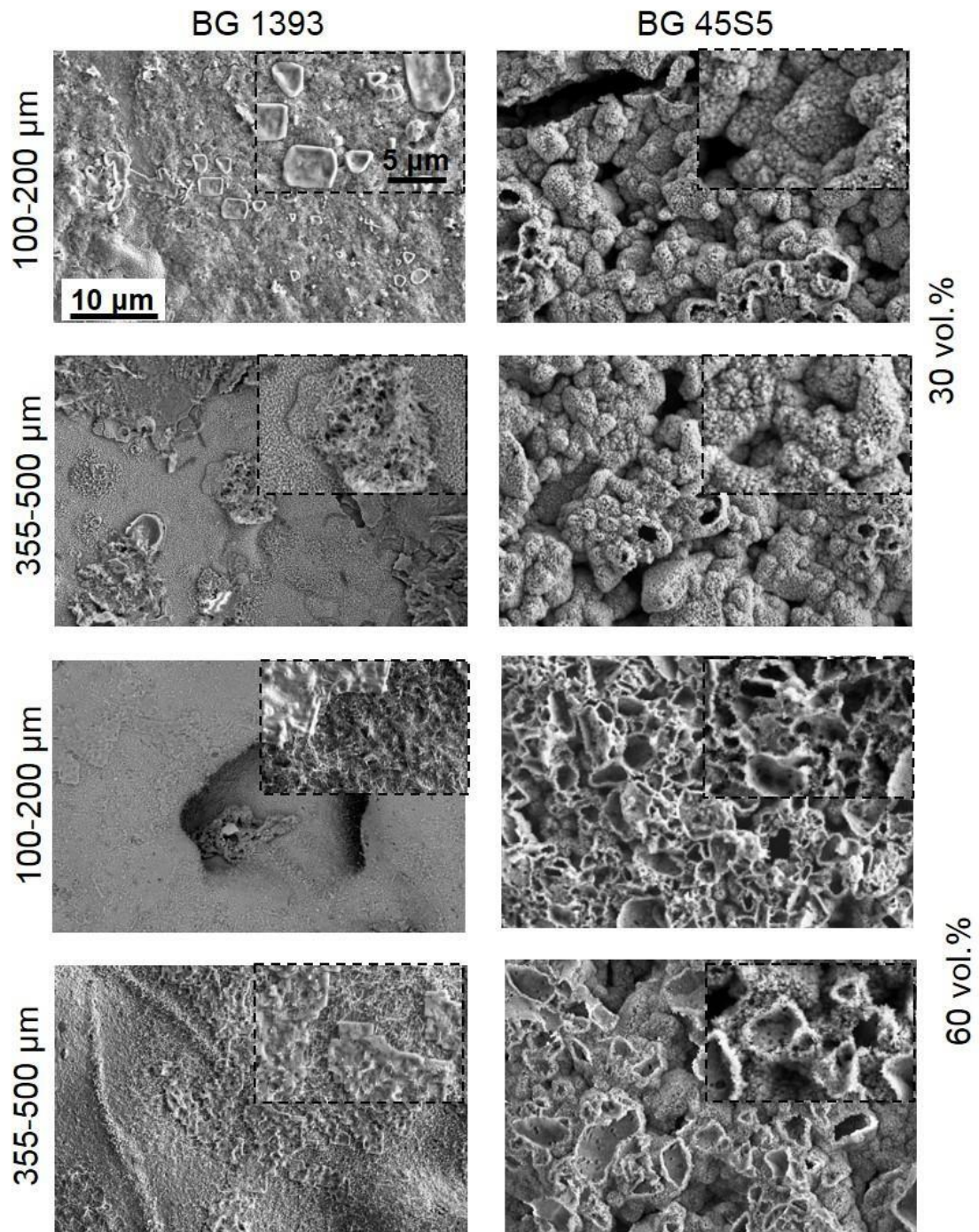
Figure 10. SEM images of the coated c.p. Ti substrates after 21 days of immersion in SBF: BG 1393 and BG 45S5. Inset: higher magnification images. Common scale bars.

Table 6. Chemical composition of BGs coated c.p. Ti obtained by EDS-SEM for the studied samples after 21 days immersed in SBF. Influence of the porosity of the substrate and BG coating in HA formation (Ca/P = 1.67). **Note:** fully-dense (FD) and space-holder size distribution is in μm.

% At.	BG 45S5					BG 1393				
	21 days in SBF									
		30 %		60 %			30 %		60 %	
	FD	100-200	355-500	100-200	355-500	FD	100-200	355-500	100-200	355-500
Ca	4.9	32.0	60.9	61.3	58.0	1.2	16.3	2.8	55.2	0.45
P	2.5	16.8	39.1	37.3	41.0	0.6	2.9	2.7	39.3	0.3
Si	1.9	0.03	≤ 0.00	1.24	0.78	4.1	12.5	25.0	3.8	0.4
Ca/P	1.98	1.91	1.56	1.64	1.41	1.76	2.16	1.02	1.40	1.56
% Discrepancy HA stoichiometry	19	14	7	2	16	5	29	39	16	7

Due to the roughness of the surfaces and the limitations of EDS-SEM, to further investigate and identify phases formed on the surface, XRD were performed (Figure 10). These results also corroborated the calcium phosphates formation on the surfaces of the samples and the dissolution of the BGs. As it was expected, calcium phosphates with different stoichiometries were found, $Ca_5(PO_4)_3(OH)$, which corresponded to HA, and $Ca_3(PO_4)_2$, among others. Despite of the crystallinity, the formation of HA was significantly higher in BG 45S5-coated c.p. Ti, particularly when using 30 vol. % of porosity and near independently on the pores size distribution, which was justified by the chemical composition of the BG. In the case of BG 1393 coated samples, substrates with 60 vol. % porosity and a pores size distribution of 100-200 μm showed the highest concentration of HA. These differences were due to the higher specific surface area, which favored the formation of HA and other calcium phosphates.

The formation of TiO_2, usual in c.p. Ti [34], and Ti_6O on the Ti surface were also remarkable. This phenomenon was previously reported, confirming that Ti_6O substoichiometry phase could be formed due to interstitial oxygen diffusion in the c.p. Ti [45].
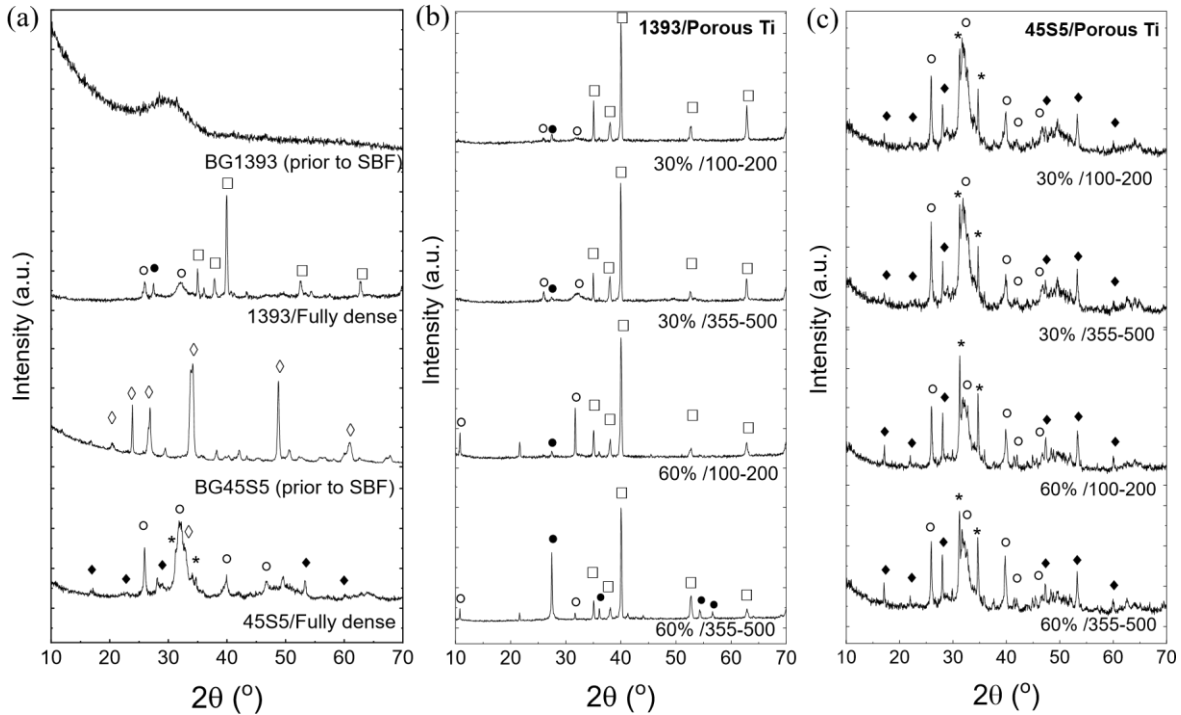

Figure 11. XRD patterns of BG powder and BG coated c.p. Ti substrates before and after 21 days of immersion in SBF: (a) BG and fully-dense c.p. Ti, (b) BG 1393/porous c.p. Ti and (c) BG 45S5/porous c.p. Ti (◊ crystalized-45S5, $Na_2CaSi_2O_6$; * TiO_2-monoclinic; ● TiO_2-rutile; □ Ti_6O; ○ $Ca_5(PO_4)_3(H)$; ♦ $Ca_3(PO_4)_2$).

The behavior observed in the present work allow us to verify that BG 1393 adheres better to the substrate, while BG 45S5 is more bioactive. The authors have recently used these preliminary assumptions to design a two-layer BG coating. The results presented here allow us not only to know the individual behavior of each type of coatings, but also to compare them in detail with the proposed BG 45S5 – BG 1393 bilayer coating [32,33].

4. Conclusions

The micro-mechanical behavior and bioactivity of BG coated porous c.p. Ti were analyzed. Porosity percentage, pore range size and interconnectivity among them in the c.p. Ti substrates allowed to solve the stress-shielding phenomenon (achieving manufacturing of implants with optimal rigidity properties close to those of cortical bone tissue), as well as favoring the transport of nutrients, bone in-growth inward and/or infiltration of coatings. To enhance the osseointegration capability of the c.p. Ti porous structures, two different BG coatings were deposited. 29Si MAS NMR studies carried out with both glasses demonstrated a higher bioactivity for BG 45S5 respect to BG 1393. However, BG 1393 coating showed higher micro-mechanical properties in comparison with BG 45S5. Additionally, larger and interconnected pores made the BGs infiltration easier, although the nature of the BG and temperature during thermal treatment also influence, since it provides to the BGs the right viscosity to flow and penetrate inside the pores. Also, the adhesion of the BGs to the pores would depend on the CTE better for BG 1393 due to its similar CTE to the c.p. Ti.

The micromechanical behavior also depended on the differences of the stiffness and hardness values of the coating - substrate system in each zone where the indentation was performed (BGs coating on c.p. Ti substrate flat area or on a porous area of the substrate). In the case of BGs coatings, results were expected, considering their nature and density. In this sense, BG 1393 is denser with a glassy appearance, while BG 45S5 coatings showed a coral and sponge-like morphologies.

The tests performed with SBF confirmed the formation of HA and calcium phosphates in both coated samples, which were favored in porous samples as the BG specific surface area exposed to SBF was higher. Additionally, despite of the crystallinity of BG 45S5 coatings, the formation of HA and calcium phosphates was more significant than in samples coated with BG 1393. Particularly, this HA formation was remarkable when

using a porosity of 30 vol. %, near independently on the pores size distribution, which was attributed to the coral-like structure that increases the specific surface area. In this sense, for the same pore size distribution, after 21 days in SBF, the amount of Ca and P in substrates coated by BG 1393 were very similar to the initial values ($\sim$ 74 and 39 mg/L, respectively), independently of the porosity percentage and pore range size. However, in the case of coating with BG 45S5, an influence of these parameters was observed, showing that the porosity percentage had higher effects than the pore size.

References

[1]   M. Marczewski, A. Miklaszewski, M. Jurczyk, Structure evolution analysis in ultrafine-grained Zr and Nb-based beta titanium alloys, J. Alloys Compd. 765 (2018) 459–469. https://doi.org/10.1016/j.jallcom.2018.06.224.

[2]   H. Jaber, T. Kovacs, Selective laser melting of Ti alloys and hydroxyapatite for tissue engineering: Progress and challenges, Mater. Res. Express. 6 (2019). https://doi.org/10.1088/2053-1591/ab1dee.

[3]   X.Y. Zhang, G. Fang, S. Leeflang, A.A. Zadpoor, J. Zhou, Topological design, permeability and mechanical behavior of additively manufactured functionally

graded porous metallic biomaterials, Acta Biomater. 84 (2019) 437–452.

https://doi.org/10.1016/j.actbio.2018.12.013.

[4]   K. Bari, A. Arjunan, Extra low interstitial titanium based fully porous

morphological bone scaffolds manufactured using selective laser melting, J.

Mech.   Behav.   Biomed.   Mater.   95   (2019)   1–12.

https://doi.org/10.1016/j.jmbbm.2019.03.025.

[5]   C. Chen, Y. Hao, X. Bai, J. Ni, S.M. Chung, F. Liu, I.S. Lee, 3D printed porous

Ti6Al4V cage: Effects of additive angle on surface properties and

biocompatibility; bone ingrowth in Beagle tibia model, Mater. Des. 175 (2019)

107824. https://doi.org/10.1016/j.matdes.2019.107824.

[6]   Y. Guo, J. Guan, H. Peng, X. Shu, L. Chen, H. Guo, Tightly adhered silk

fibroin coatings on Ti6Al4V biometals for improved wettability and compatible

mechanical properties, Mater. Des. 175 (2019) 107825.

https://doi.org/10.1016/j.matdes.2019.107825.

[7]   G. Fernandez de Grado, L. Keller, Y. Idoux-Gillet, Q. Wagner, A.M. Musset, N.

Benkirane-Jessel, F. Bornert, D. Offner, Bone substitutes: a review of their

characteristics, clinical use, and perspectives for large bone defects

management, J. Tissue Eng. 9 (2018).

https://doi.org/10.1177/2041731418776819.

[8]   C.D.F. Moreira, S.M. Carvalho, R.G. Sousa, H.S. Mansur, M.M. Pereira,

Nanostructured chitosan/gelatin/bioactive glass in situ forming hydrogel

composites as a potential injectable matrix for bone tissue engineering, Mater.

Chem. Phys. 218 (2018) 304–316.

https://doi.org/10.1016/j.matchemphys.2018.07.039.

[9]   K. Vuornos, M. Ojansivu, J.T. Koivisto, H. Häkkänen, B. Belay, T. Montonen,

H. Huhtala, M. Kääriäinen, L. Hupa, M. Kellomäki, J. Hyttinen, J.A. Ihalainen, S. Miettinen, Bioactive glass ions induce efficient osteogenic differentiation of human adipose stem cells encapsulated in gellan gum and collagen type I hydrogels, Mater. Sci. Eng. C. 99 (2019) 905–918. https://doi.org/10.1016/j.msec.2019.02.035.

[10]   A. Ali, M. Ershad, V.K. Vyas, S.K. Hira, P.P. Manna, B.N. Singh, S. Yadav, P. Srivastava, S.P. Singh, R. Pyare, Studies on effect of CuO addition on mechanical properties and in vitro cytocompatibility in 1393 bioactive glass scaffold, Mater. Sci. Eng. C. 93 (2018) 341–355. https://doi.org/10.1016/j.msec.2018.08.003.

[11]   N.H. Cohrs, K. Schulz-Schönhagen, D. Mohn, P. Wolint, G. Meier Bürgisser, W.J. Stark, J. Buschmann, Modification of silicone elastomers with Bioglass 45S5® increases in ovo tissue biointegration, J. Biomed. Mater. Res. - Part B Appl. Biomater. 107 (2019) 1180–1188. https://doi.org/10.1002/jbm.b.34211.

[12]   J. Zhang, R.J.M. Lynch, T.F. Watson, A. Banerjee, Chitosan-bioglass complexes promote subsurface remineralisation of incipient human carious enamel lesions, J. Dent. 84 (2019) 67–75. https://doi.org/10.1016/j.jdent.2019.03.006.

[13]   A.S. Bakry, M.A. Abbassy, The efficacy of a bioglass (45S5)paste temporary filling used to remineralize enamel surfaces prior to bonding procedures, J. Dent. 85 (2019) 33–38. https://doi.org/10.1016/j.jdent.2019.04.010.

[14]   M. Rasti, S. Hesaraki, N. Nezafati, Effects of GPTMS concentration and powder to liquid ratio on the flowability and biodegradation behaviors of 45S5 bioglass/tragacanth bioactive composite pastes, J. Appl. Polym. Sci. 136 (2019) 17–22. https://doi.org/10.1002/app.47604.

[15] A. Civantos, C. Domínguez, R.J. Pino, G. Setti, J.J. Pavón, E. Martínez-Campos,
F.J. Garcia Garcia, J.A. Rodríguez, J.P. Allain, Y. Torres, Designing bioactive

porous titanium interfaces to balance mechanical properties and in vitro cells

behavior towards increased osseointegration, Surf. Coatings Technol. 368

(2019)

162–174. https://doi.org/10.1016/j.surfcoat.2019.03.001.

[16] C. Domínguez-Trujillo, F. Ternero, J.A. Rodríguez-Ortiz, J.J. Pavón, I.

Montealegre-Meléndez, C. Arévalo, F. García-Moreno, Y. Torres, Improvement

of the balance between a reduced stress shielding and bone ingrowth by

bioactive coatings onto porous titanium substrates, Surf. Coatings Technol. 338

(2018) 32–

37. https://doi.org/10.1016/j.surfcoat.2018.01.019.

[17] S. Lascano, C. Arévalo, I. Montealegre-Melendez, S. Muñoz, J.A. Rodriguez-

Ortiz, P. Trueba, Y. Torres, Porous titanium for biomedical applications:

Evaluation of the conventional powder metallurgy frontier and space-holder

technique, Appl. Sci. 9 (2019). https://doi.org/10.3390/app9050982.

[18] Standard Test Method for ASTM C373-14, Standard Test Method for Water

Absorption, Bulk Density, Apparent Porosity, and Apparent Specific Gravity of

Fired Whiteware Products, Ceramic Tiles, and Glass Tiles, West

Conshohocken, PA, 2014. https://doi.org/10.1520/C0373-14.

[19] A.M. Beltrán, A. Civantos, C. Dominguez-Trujillo, R. Moriche, J.A.
Rodríguez-

Ortiz, F. García-Moreno, T.J. Webster, P.H. Kamm, A.M. Restrepo, Y. Torres,

Porous titanium surfaces to control bacteria growth: Mechanical properties and

sulfonated polyetheretherketone coatings as antibiofouling approaches, Metals

(Basel). 9 (2019). https://doi.org/10.3390/met9090995.

[20] L. Hemmouche, D. Chicot, A. Amrouche, A. Iost, M.A. Belouchrani, X. Decoopman, G. Louis, E.S. Puchi-Cabrera, An analysis of the elastic properties of a porous aluminium oxide film by means of indentation techniques, Mater. Sci. Eng. A. 585 (2013) 155–164. https://doi.org/10.1016/j.msea.2013.07.054.

[21] W.C. Oliver, G.M. Pharr, Measurement of hardness and elastic modulus by instrumented indentation: Advances in understanding and refinements to methodology, J. Mater. Res. 19 (2004) 3–20. https://doi.org/10.1557/jmr.2004.19.1.3.

[22] ISO 23317:2014, Implants for surgery — In vitro evaluation for apatite-forming ability of implant materials. International Standard, Switzerland, 2014, www.iso.org, (n.d.).

[23] J.R. Jones, Reprint of: Review of bioactive glass: From Hench to hybrids, Acta Biomater. 23 (2015) S53–S82. https://doi.org/10.1016/j.actbio.2015.07.019.

[24] B. Zagrajczuk, M. Dziadek, Z. Olejniczak, K. Cholewa-Kowalska, M. Laczka, Structural and chemical investigation of the gel-derived bioactive materials from the SiO2–CaO and SiO2-CaO-P2O5 systems, Ceram. Int. 43 (2017) 12742– 12754. https://doi.org/10.1016/j.ceramint.2017.06.160.

[25] J. Xiao, Y. Wan, F. Yao, Y. Huang, Y. Zhu, Z. Yang, H. Luo, Constructing 3D scaffold with 40-nm-diameter hollow mesoporous bioactive glass nanofibers, Mater. Lett. 248 (2019) 201–203. https://doi.org/10.1016/j.matlet.2019.04.041.

[26] X. Ma, H. Wang, H. Xie, J. Qu, X. Chen, F. Chen, Q. Song, H. Yin, Engineering the porosity and superelastic behaviors of NiTi alloys prepared by an electroassisted powder metallurgical route in molten salts, J. Alloys Compd. 794 (2019) 455–464. https://doi.org/10.1016/j.jallcom.2019.04.166.

[27] H. Liang, Y. Yang, D. Xie, L. Li, N. Mao, C. Wang, Z. Tian, Q. Jiang, L. Shen, Trabecular-like Ti-6Al-4V scaffolds for orthopedic: fabrication by selective

laser melting and in vitro biocompatibility, J. Mater. Sci. Technol. 35 (2019) 1284–

1297. https://doi.org/10.1016/j.jmst.2019.01.012.

[28] H.-D. Zheng, L.-L. Liu, C.-L. Deng, Z.-F. Shi, C.-Y. Ning, Mechanical

properties of AM Ti6Al4V porous scaffolds with various cell structures, Rare

Met. 38 (2019) 561–570. https://doi.org/10.1007/s12598-019-01231-4.

[29] H. Eckert, Structural characterization of bioactive glasses by solid state NMR,

J. Sol-Gel Sci. Technol. 88 (2018) 263–295. https://doi.org/10.1007/s10971-

0184795-7.

[30] P. Balasubramanian, A.J. Salinas, S. Sanchez-Salcedo, R. Detsch, M.

ValletRegi, A.R. Boccaccini, Induction of VEGF secretion from bone marrow

stromal cell line (ST-2) by the dissolution products of mesoporous silica glass

particles containing CuO and SrO, J. Non. Cryst. Solids. 500 (2018) 217–224.

https://doi.org/10.1016/j.jnoncrysol.2018.07.073.

[31] M.W.G. Lockyer, D. Holland, R. Dupree, NMR investigation of the structure of

some bioactive and related glasses, J. Non. Cryst. Solids. 188 (1995) 207–219.

https://doi.org/10.1016/0022-3093(95)00188-3.

[32] A.M. Beltrán, A. Alcudia, B. Begines, J.A. Rodríguez-ortiz, Y. Torres, Porous

titanium substrates coated with a bilayer of bioactive glasses, J. Non. Cryst.

Solids. 544 (2020) 120206. https://doi.org/10.1016/j.jnoncrysol.2020.120206.

[33] A. M Beltran, B. Begines, A. Alcudia Cruz, J. A. Rodríguez-Ortiz, Y. Torres,

Biofunctional and Tribo-mechanical Behavior of Porous Titanium Substrates

Coated with a Bioactive Glass Bilayer (45S5 – 1393), AC Appl. ater. &

Interfaces. 0 (2020). https://doi.org/10.1021/acsami.0c07318.

[34] H. Elsayed, G. Brunello, C. Gardin, L. Ferroni, D. Badocco, P. Pastore, S. Sivolella, B. Zavan, L. Biasetto, Bioactive sphene-based ceramic coatings on cpTi substrates for dental implants: An in vitro study, Materials (Basel). 11 (2018). https://doi.org/10.3390/ma11112234.

[35] D. Bellucci, V. Cannillo, A. Sola, Coefficient of thermal expansion of bioactive glasses: Available literature data and analytical equation estimates, Ceram. Int. 37 (2011) 2963–2972. https://doi.org/10.1016/j.ceramint.2011.05.048.

[36] N. Rohr, J.B. Nebe, F. Schmidli, P. Müller, M. Weber, H. Fischer, J. Fischer, Influence of bioactive glass-coating of zirconia implant surfaces on human osteoblast behavior in vitro, Dent. Mater. 35 (2019) 862–870. https://doi.org/10.1016/j.dental.2019.02.029.

[37] O. Rodriguez, A. Matinmanesh, S. Phull, E. Schemitsch, P. Zalzal, O. Clarkin, M. Papini, M. Towler, Silica-Based and Borate-Based, Titania-Containing Bioactive Coatings Characterization: Critical Strain Energy Release Rate, Residual Stresses, Hardness, and Thermal Expansion, J. Funct. Biomater. 7 (2016) 32. https://doi.org/10.3390/jfb7040032.

[38] H.R. Fernandes, A. Gaddam, A. Rebelo, D. Brazete, G.E. Stan, J.M.F. Ferreira, Bioactive glasses and glass-ceramics for healthcare applications in bone regeneration and tissue engineering, Materials (Basel). 11 (2018) 1–54. https://doi.org/10.3390/ma11122530.

[39] F. Baino, E. Fiume, Mechanical characterization of 45S5 bioactive glass-derived scaffolds, Mater. Lett. 245 (2019) 14–17. https://doi.org/10.1016/j.matlet.2019.02.086.

[40] C. Domínguez-Trujillo, F. Ternero, J.A. Rodríguez-Ortiz, S. Heise, A.R. Boccaccini, J. Lebrato, Y. Torres, Bioactive coatings on porous titanium for biomedical applications, Surf. Coatings Technol. 349 (2018) 584–592.

https://doi.org/10.1016/j.surfcoat.2018.06.037.

[41] F. Abushahba, E. Söderling, L. Aalto-Setälä, J. Sangder, L. Hupa, T.O. Närhi,

Antibacterial properties of bioactive glass particle abraded titanium against

Streptococcus mutans, Biomed. Phys. Eng. Express. 4 (2018) 45002.

https://doi.org/10.1088/2057-1976/aabeee.

[42] D. Bellucci, V. Cannillo, A. Sola, An overview of the effects of thermal

processing on bioactive glasses, Sci. Sinter. 42 (2010) 307–320.

https://doi.org/10.2298/SOS1003307B.

[43] S. Hosseini, H. Farnoush, Characterization and in vitro bioactivity of

electrophoretically deposited Mn-modified bioglass-alginate nanostructured

composite coatings, Mater. Res. Express. 6 (2019).

https://doi.org/10.1088/20531591/aaedfe.

[44] R.I.M. Asri, W.S.W. Harun, M.A. Hassan, S.A.C. Ghani, Z. Buyong, A review

of hydroxyapatite-based coating techniques: Sol-gel and electrochemical

depositions on biocompatible metals, J. Mech. Behav. Biomed. Mater. 57

(2016) 95–108. https://doi.org/10.1016/j.jmbbm.2015.11.031.

[45] M.L. dos Santos, C. dos Santos Riccardi, E. de Almeida Filho, A.C. Guastaldi,

Calcium phosphates of biological importance based coatings deposited on

Ti15Mo alloy modified by laser beam irradiation for dental and orthopedic

applications, Ceram. Int. 44 (2018) 22432–22438.

https://doi.org/10.1016/j.ceramint.2018.09.010.